Pure Appl. Chem., Vol. 74, No. 9, pp. 1675–1692, 2002.

Some properties of spherical and rod-shaped semiconductor and metal nanocrystals*

Christy F. Landes, Stephan Link, Mona B. Mohamed, Babak Nikoobakht, and Mostafa A. El-Sayed‡

Laser Dynamics Laboratory, School of Chemistry and Biochemistry, Georgia Institute of Technology, Atlanta, GA 30332-0400, USA

Abstract: In this paper, we summarize our results on the effect of changing size and shape of semiconductor and metallic nanocrystals. The change in size (from 3.5 to 1.1 nm) and shape (from spherical to rod) of CdSe nanocrystals is found to affect both their optical and nonradiative properties. In gold quasi-spherical nanocrystals, results on the dependence of the electron-phonon relaxation of the surrounding medium are presented. For gold nanorods, results and conclusions on the mechanism of their self-assembly are presented. Enhanced Raman scattering on their surfaces is studied and compared with that on spherical particle surfaces.

INTRODUCTION

A great deal of studies have been carried out on the effect of changing the size of semiconductor nanoparticles (NPs) on their properties [1–3]. As their size decreases to their Bohr radius (usually around a few nanometers), all electronic properties change, and equally important, become dependent on size. In this size, a semiconductor–nanoparticle transition occurs in which the electrons and holes are confined beyond their natural Bohr radius. The properties become dependent not only on size, but also on shape. For example, if an electron-hole pair (i.e., an exciton) is formed in a sphere and in a space equal to or smaller than its natural separation, there is no room for the exciton to move. This is a system called a "quantum dot", as its exciton has zero degrees of freedom for its motion (in other words, the exciton is confined in all three dimensions). If the particle is elongated, for example, along the *z*-axis, the exciton formed will still be confined in the *x* and y directions, but can be transported along *z*. This suggests that it is confined in two directions, but can move in one direction. If, on the other hand, the original sphere is compressed along *z* and extended equally in *x* and *y* (e.g., in nanodisks), the exciton's motion is confined in one direction (*z*), but has room to move along *x* and *y*, i.e., in two dimensions. All these shape changes must have effects on the optical and radiative properties of semiconductor NPs. These changes are discussed for CdSe upon changing its size to the NP-molecular size transition in the section "Changes in the properties of CdSe nanoparticles as their size decreases to the 1-nm limit" and upon changing its shape from spherical to rods in the section "Shape-dependent optical properties and ultrafast charge carrier dynamics of CdSe nanocrystals".

Noble metals of small spherical size are known to have a very strong visible absorption owing to the resonant coherent oscillation of the free electrons in the conduction band [4–6] (the brilliant rose color in stained glass windows of cathedrals built in the 17th century is due to the strong absorption of gold NPs). If the particle is not spherical, e.g., rod-shaped, the optical (absorption and fluorescence), nonradiative, and physical properties of these gold nanorods (NRs) become quite different from those

Pure Appl. Chem.* **74, 1489–1783 (2002). An issue of reviews and research papers based on lectures presented at the 2nd IUPAC Workshop on Advanced Materials (WAM II), Bangalore, India, 13–16 February 2002, on the theme of nanostructured advanced materials.

‡Corresponding author

of spherical ones [4,5]. In the present account, the changes in the nonradiative relaxation are discussed in the section "Ultrafast electron dynamics in gold nanoparticles embedded in different media". In the last section, the mechanism of the rod self-assembly and the surface Raman enhancement of adsorbed molecules on their surfaces are compared with those of spheres.

SEMICONDUCTOR NANOPARTICLES

Changes in the properties of CdSe nanoparticles as their size decreases to the 1-nm limit

The relationship between size, shape, and surface is very apparent when the NP size has been reduced to what might be considered a molecular limit. In very small NPs, the irregular NP surface dominates the carrier relaxation pathways, overall NP shape, and overall NP stability.

NP size and surface quality can be examined with fluorescence spectroscopy. NPs that fluoresce with a narrow linewidth and small Stokes shift are dominated by what is referred to as near band-gap emission [1], and are characterized by a generally continuous surface with most surface atoms exhibiting the coordination and oxidation state of their bulk counterparts. In contrast, NPs that emit broadly with a larger Stokes shift are considered to exhibit deep-trap emission [2]. Deep-trap emission has been characterized as emission from the recombination of trapped electrons and holes with broad energy distributions. Carrier traps result from surface irregularities such as missing atoms, uncommon oxidation states, or adsorbed impurities [3,7,8]. When the NP size is reduced such that the particle is essentially all surface, the curvature of the surface is so high that virtually all of the surface atoms have a slightly different coordination and/or effective oxidation state. The experimental and theoretical studies of very small (1–2 nm) CdS [9,10] and CdSe [11–13] NPs are examples of such NP systems that are dominated by surface interactions. These small NPs emit light that is characteristic of deep-trap luminescence, unless they are overcoated with a wider band-gap material such as ZnS [14], which confines the carriers to the CdSe core.

NP size can also be related to physical shape and stability. Large NPs are approximately spherical, but the asymmetry of the wurtzite lattice structure causes a slight elongation along the *c*-axis that is observed as a prolate deviation from a perfect spherical shape. This has been exploited in the recent preparations of CdSe NRs that enhance the elongation along the asymmetric axis [15–17]. Very small NPs, composed of fewer than 1000 atoms, exhibit an even stronger deviation from spherical symmetry, and form, for example, tetrahedral particle shapes [11–13]. Also, because smaller NPs tend to form tetrahedral shapes, there are only certain Cd_xSe_y combinations that provide tetrahedral shapes, and these conformations would be expected to be much more stable than structures slightly larger or smaller. This notion is derived from the extensive work in metal clusters where certain "magic number" structures with enhanced stability are well known [18].

Also, very small NPs can deviate from larger NPs in the relative stability of the crystal lattice. For example, Eichkorn and Ahlrichs have modeled the optimized structures of small CdSe clusters [13], and their calculations suggested that, depending on the size of the cluster, either the zinc blend or the wurtzite lattice was most stable. Additionally, phase transformations have been shown to be dependent on the original NP size and surface. Tolbert and Alivisatos showed [19] that the pressure-induced transformation between wurtzite and rock salt structures in very small semiconductor NPs was highly dependent on surface interactions. The group found that altering the pressure medium for these small NPs had a large effect on the value of the barrier energy for phase transformation. Thus, solvent and capping interactions are important determinants for phase stability in small NPs.

The work described herein relates the NP size and surface to fluorescence properties [20,21], physical stability [22], and electronic structure. The molecular hole acceptor, *n*-butylamine, is used as a surface adsorbate. Adsorption of amine to the NP surface induces size-dependent changes in the NP fluorescence and causes a transformation in very small NPs toward a magic number structure.

Colloidal CdSe NPs capped with trioctylphosphine oxide (TOPO) and trioctylphosphine (TOP) were prepared from $(CH_3)_2Cd$ and Se precursors as described by Murray et al. [7] with modifications described by Landes et al. [21,22] necessary to stabilize small NPs. Fluorescence and electronic absorption measurements were performed as described elsewhere [20–22].

Figure 1 illustrates the electronic absorption and steady-state fluorescence spectra of a series of CdSe NPs ranging in size from 3.2 nm (a) to 2.3 nm (b) to 1.6 nm (c). The fluorescence of the 3.2-nm NPs shown in Fig 1a is characteristic of near band-edge exciton type fluorescence, or shallow-trap fluorescence. The fluorescence has a small Stokes shift and is highly symmetrical with respect to the lowest energy absorption feature. Fluorescence from 2.3-nm NPs is shown in Fig. 1b. This intermediate-size NP emits with both near band-edge emission and deep-trap emission. Deep-trap emission in the 2.3-nm NPs is greatly Stokes-shifted with respect to the band edge and is very broad with respect to the inhomogeneously broadened sample size. The 1.6-nm NP fluorescence, shown in Fig. 1c., is dominated by deep-trap emission, and no band-edge emission is observed. 1.6-nm NPs are composed almost entirely of irregularly spaced surface atoms, and these atoms dominate the fluorescence.

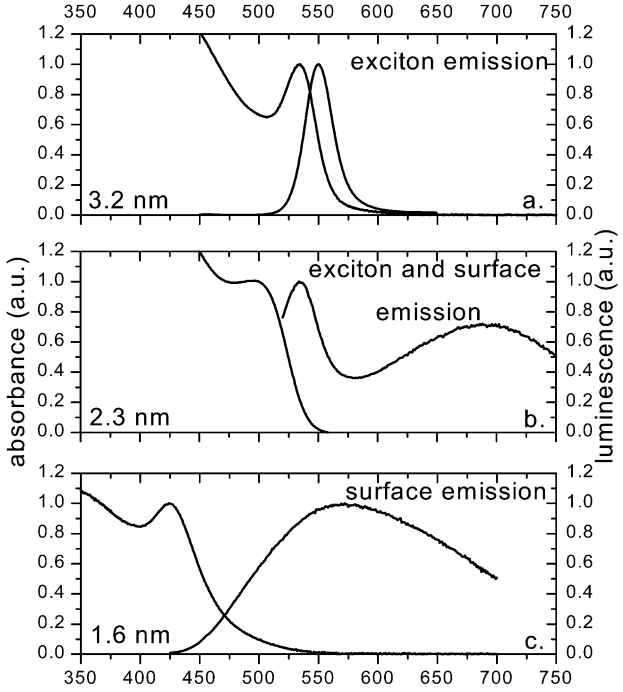

Fig. 1 Electronic absorption spectra for 3.2-, 2.3-, and 1.6-nm NPs are shown on the left axis in a, b, and c, respectively. On the right axis, fluorescence spectra for each size are shown. (a) One can observe that the larger 3.2-nm NPs fluoresce with exciton, or near band-edge emission. (b) The 2.3-nm NPs exhibit exciton emission, but the introduction of surface irregularities in these NPs leads to deep-trap-type surface emission as well. (c) The smallest 1.6-nm NPs emit light exclusively by deep-trap-type emission from a multitude of surface states.

Steady-state and fluorescence spectra of 3.2-nm and 1.6-nm NPs alone and in the presence of *n*-butylamine are shown in Fig. 2. Fluorescence decays are included in the insets. Butylamine quenches the fluorescence yield of 3.2-nm NPs, as seen in Fig. 2a, however, the inset shows that the lifetimes are not quenched. In contrast, as observed in Fig. 2b, fluorescence from 1.6-nm NPs is quenched more dra-

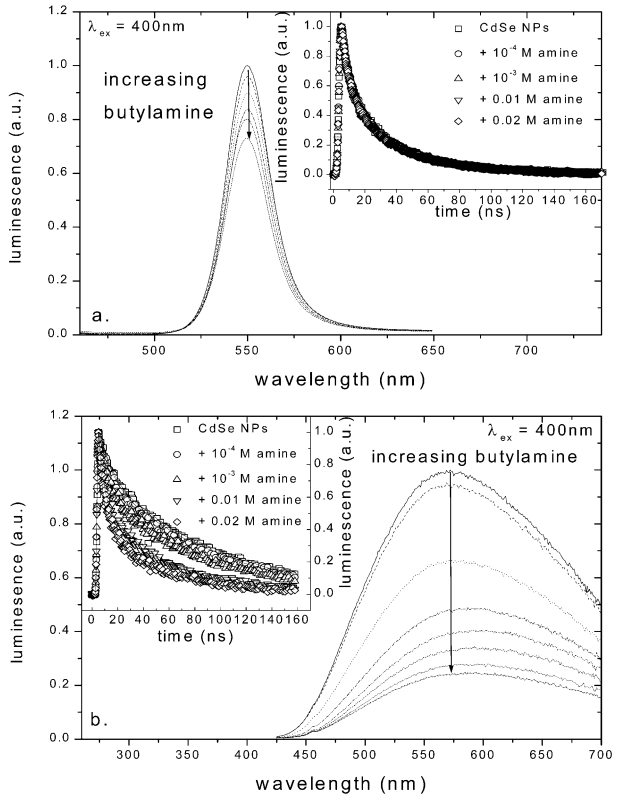

Fig. 2 In the presence of a simple hole acceptor, *n*-butylamine, the fluorescence of 3.2- and 2.3-nm NPs is quenched differently. (a) The steady-state luminescence of 3.2-nm NPs is quenched by the addition of increasing amounts of butylamine. The inset shows that the fluorescence lifetimes of the NPs are not quenched. It was suggested that the butylamine binds with the NP surface and competes with population of emitting states, and disables the emission process in these NPs. (b) The quenching of deep-trap luminescence of 1.6-nm NPs is shown. The inset illustrates that the fluorescence lifetimes of the small NPs are quenched by the amine. The amine can quench the less-allowed deep-trap fluorescence of the smaller NPs by competing with the relaxation process through excited-state electron transfer.

matically, and the lifetimes are also quenched, as the inset shows. The different quenching behavior of the two different sizes can be used to describe the mechanism of fluorescence in each case.

Electronic absorption spectra of 3.2-nm and 1.6-nm NPs alone and in the presence of higher concentrations of butylamine than used for the quenching experiments are shown in Fig. 3. The addition of the amine to 3.2-nm NPs, as shown in Fig. 3a, does not affect the electronic structure of the NPs. When larger amounts of amine are added to 1.6-nm NPs, dramatic changes in the electronic structure are observed, as seen in Fig. 3b. As greater amounts of amine are added to the 1.6-nm NPs, the original absorption feature decreases, and a new absorption feature grows at 414 nm. The new feature exhibits much higher monodispersity than the original feature, as evidenced by the narrower absorption linewidth. Additionally, the presence of an isobestic point suggests that this conversion is due to an equilibrium process between two species.

The fluorescence from 3.2-nm NPs, shown in Fig. 1a, is primarily from the band-edge. The lack of spectral broadening and the relatively fast lifetime (<30 ns), suggest that the transition is highly allowed and that there is little competition from deep-trapping processes. That butylamine quenches the overall quantum yield of the 3.2-nm fluorescence, but does not affect the lifetime, as seen in Fig. 2a,

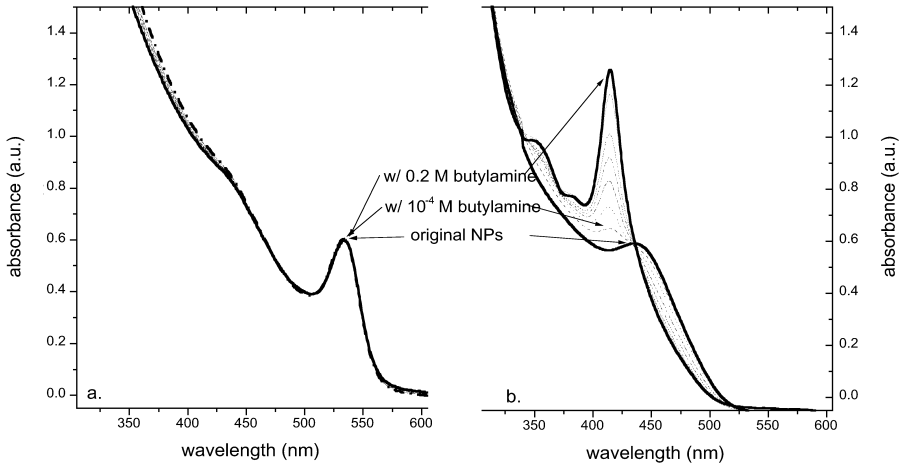

Fig. 3 (a) The electronic absorption for 3.2-nm NPs is shown, along with the spectra of the NPs with increasing amounts of *n*-butylamine. No significant change can be observed in the spectra, indicating that although the amine adsorbs to the NP surface, this adsorption does not change the overall electronic structure of the NPs. (b) The electronic absorption for 1.6-nm NPs is shown. In contrast to the larger particles, as increasing amounts of amine are added, the original broad absorption decreases, and a new narrower feature, centered at 414 nm, appears. This indicates a narrowing in the size distribution, and the presence of the isobestic point suggests that the transformation is an equilibrium process. The change in the electronic structure indicates that the adsorption of butylamine induces either a size or a phase change, or some combination.

indicates that the amine competes with the population of emission centers, but not with the actual emission process. By adsorbing to the NP surface, the amine blocks the emission pathway of the NPs to which it has adsorbed, and decreases the number of emitting species, but not the process by which the fluorescence occurs [20]. In comparison, the fluorescence of 1.6-nm NPs occurs entirely from deep-trap processes, as shown in Fig. 1c, indicating the prevalence of surface irregularities. The fluorescence lifetime is slow, suggesting that the process is less allowed. When butylamine is added, both the fluorescence quantum yield and the lifetime are quenched, as shown in Fig. 2b. That the butylamine quenches both the lifetime and the yield indicates that, unlike in larger NPs, quenching occurs through an electron-transfer process. By binding to the small NP surface, the amine not only blocks the population of the emitting sites as in larger NPs, it also competes with the fluorescence process by undergoing excited-state electron transfer with the NP. This process becomes energetically allowed in the smaller NPs because it provides a more efficient relaxation route with respect to the less-allowed deep-trap fluorescence [21].

In 3.2-nm NPs, surface interactions can affect the relaxation process, as shown in Figs. 1 and 2, but the predominance of bulk atoms governs the electronic structure and particle stability. This can be seen in Fig. 3a, wherein the electronic absorption spectra of 3.2-nm NPs is observed to be unchanged by the addition of *n*-butylamine. Butylamine induces a dramatic transformation in the electronic structure of the 1.6-nm NPs, however, as observed in Fig. 3b. The clear isobestic point suggests that this transformation occurs as an equilibrium process between two species. The resulting NPs, absorbing at 414 nm, are consistent with a stable magic number structure that has been observed by others in this size range [7,23]. It was suggested, in [22], that the adsorption of butylamine to the NP surface results in the release of heat, which induces the transformation of the small NPs into a magic number structure. This transformation could involve resizing, as suggested by the narrowing and blue-shift of the electronic spectrum. Alternately, the transformation could involve a phase transformation from a wurtzite lattice to a stable zinc-blend structure predicted by Eichkorn and Ahlrichs [13]. Finally, the

transformation could involve both types of process. Regardless, it is clear from the electronic absorption spectra in Fig. 3 that the stability, physical size/shape, and electronic structure of very small NPs are governed by the surface.

In conclusion, it has been illustrated that a molecular adsorbate such as *n*-butylamine can be used to probe the relationship between size and surface in CdSe NPs. Butylamine was used to quench the fluorescence of NPs in both the small and larger-size regimes. The quenching mechanism was found to be size-dependent, with electron transfer occurring in small NPs in which deep-trap fluorescence predominates. Also, the overall stability and electronic structure of small NPs can be manipulated by using the energy released from the adsorption process to transform small NPs into a magic number structure. This process occurs because, unlike in larger NPs, surface interactions dominate not just the carrier relaxation process, but also the physical and electronic structure of the particle.

Shape-dependent optical properties and ultrafast charge carrier dynamics of CdSe nanocrystals

Controlling the shape of semiconductor nanocrystals affords an opportunity to test the theories of quantum confinement [24,25]. By elongation of the unique *c*-axis in CdSe NRs, the near degeneracy in spherical quantum dot breaks. Preliminary studies comparing the optical properties of CdSe nanodots (NDs) and that of CdSe NRs of a width comparable to the diameter of the NDs shows that the band-gap absorption of CdSe NRs depends primarily on the width and slightly on the length [26]. The unique characteristic of CdSe NRs is the highly linearly polarized emission along their long axis from even slightly elongated NRs, and the non-monotonic change of the global Stokes shift (splitting between the band-gap emission and absorption peaks) with aspect ratio [15,27]. These studies are just the beginning in discovering the role of shape in semiconductor nanocrystals. The large global Stokes shift in CdSe NRs could be very helpful in optoelectronics application such as light-emitting diodes (LEDs) and quantum dot lasers where reabsorption could be a problem.

Recently, Hu et al. [28] used the semiempirical pseudopotential method to calculate the electronic states of CdSe NRs with increasing aspect ratio. They started from a spherical dot with a certain diameter and inserted a cylindrical segment along the *c*-axis. In CdSe nanocrystals, the highest unoccupied molecular orbital (HOMO) originates from Se 4P atomic orbitals, and the lowest unoccupied molecular orbital (LUMO) from Cd 5S atomic orbitals. Excited electronic states arise by exciting an electron from an occupied Se 4P orbital to a Cd 5S orbital. These electronic states are strongly dependent on the size (the degree of confinement). Because increasing the aspect ratio only reduces confinement along the *c*-direction, some energy levels are sensitive to the length of the NR much more than others, and level crossing occurs. For HOMO levels, the levels consisting of a Se $4P_z$ component are more dependent on the length than those consisting of Se $4P_{x,y}$. By increasing the NR length, the energy levels converge into several energy levels. This is a transition from zero-dimensional confinement (0D) to one dimensional confinement (1D), where a continuous band forms along the *c*-axis. For this reason, more-versatile nanoelectronic and optical devices, which combine the advantage of 0D and 1D confinement, can potentially be made using quantum NRs as building blocks [28].

CdSe NDs are prepared according to the procedure developed by Murray et al. [7] in which a mixture of dimethyl cadmium and Se powder dissolved in TOP was injected to a hot solution of TOPO at high temperature. CdSe NRs were prepared using a similar approach. A mixture of a binary surfactant of TOPO and tetradecyl phosphonic acid (TDPA) were used instead of TOPO. This method has been developed recently by Peng et al. [15,16,29]. The freshly prepared sample of CdSe nanocrystals was analyzed by a Hitachi HF-2000 field emission transmission electron microscope (TEM) operating at 200 kV. Counting over 300 particles resulted in an average diameter of 4.2 ± 0.6 nm and an average length of 13.5 ± 1.5 nm, giving an average aspect ratio of ~3. The contamination of the sample by spherical or quasispherical CdSe nanoparticles is estimated to be less than 10 %. The absorption, emission, and TEM images of the CdSe NRs and NDs are shown in Fig. 4. Both the NDs and NRs have a band-

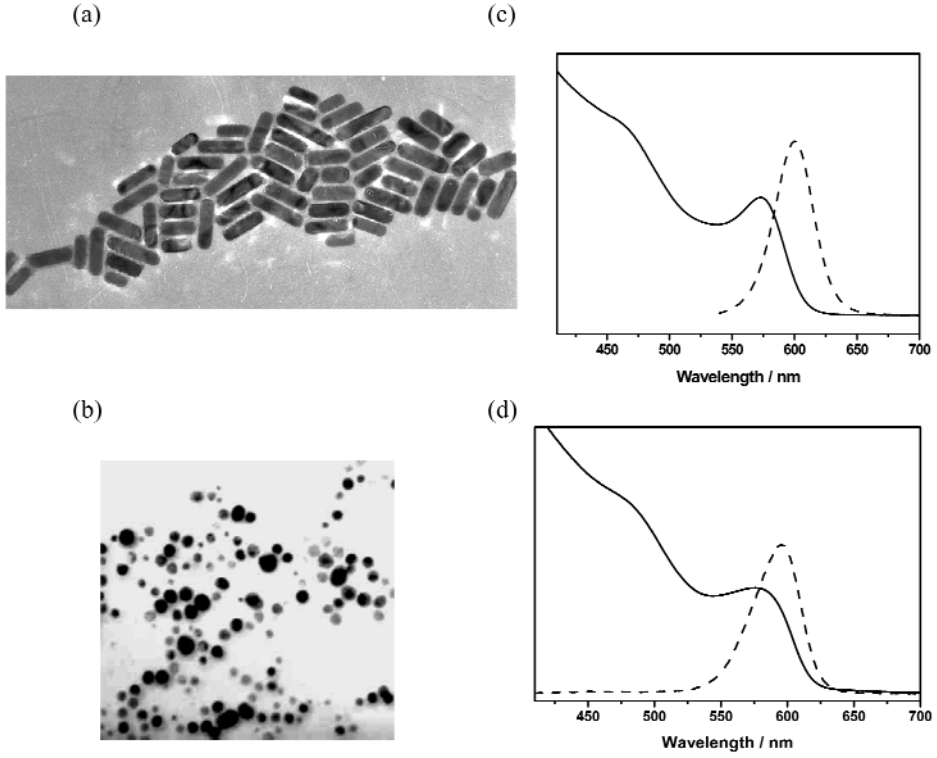

Fig. 4 TEM images of CdSe NRs (a) and NDs (b) and their absorption and emission spectra [(c) and (d), respectively].

gap absorption at 580 nm, but the band-gap emission in the case of the NRs is red-shifted with respect to the spheres.

Figure 5 compares the change in the bleach spectrum of the NRs with that of the NDs using the same delay times of 200 fs, 400 fs, 1.2 ps, and 2.4 ps in each spectrum. In both spectra, the same laser pump wavelength and energy were used [30]. The continuum white light, which was used as a probe beam, does not have much intensity below 450 nm. Thus, the spectrum could not be recorded between 400 to 450 nm. Within 200 fs, the carriers seem to distribute themselves among fewer energy states in the NDs compared to the NRs. This allows the $1S_e$-$1S_{h(3/2)}$ (band-gap state at 585 nm) to have higher population than the corresponding state in the NRs. As the delay time increases, the spectrum of the NDs does not change much, while in the NRs, the population of the higher excitonic states relaxes rapidly to the lower states and finally to the band-gap state.

Deconvolution of the bleach spectra at early time (1 ps) is shown for both the NDs and the NRs in Figs. 5c and 5d. In agreement with the size distribution results of the NDs (TEM image Fig. 4c), the bands of the NDs are much broader than those of the NRs (which have very narrow size distribution). Despite the inhomogeneous broadening in the bleach spectra of the NDs, it is clear that the NRs have more absorption bands than the NDs. This could be explained by the fact that decreasing the symmetry in the NRs leads to splitting of the corresponding degenerate excited state in the NRs. Furthermore, the energy states for the NDs are well known in the literature [31].

Femtosecond time-resolved pump-probe spectroscopy is a powerful tool to determine the rise and decay time of the population density of the different energy levels. The CdSe NRs and NDs samples

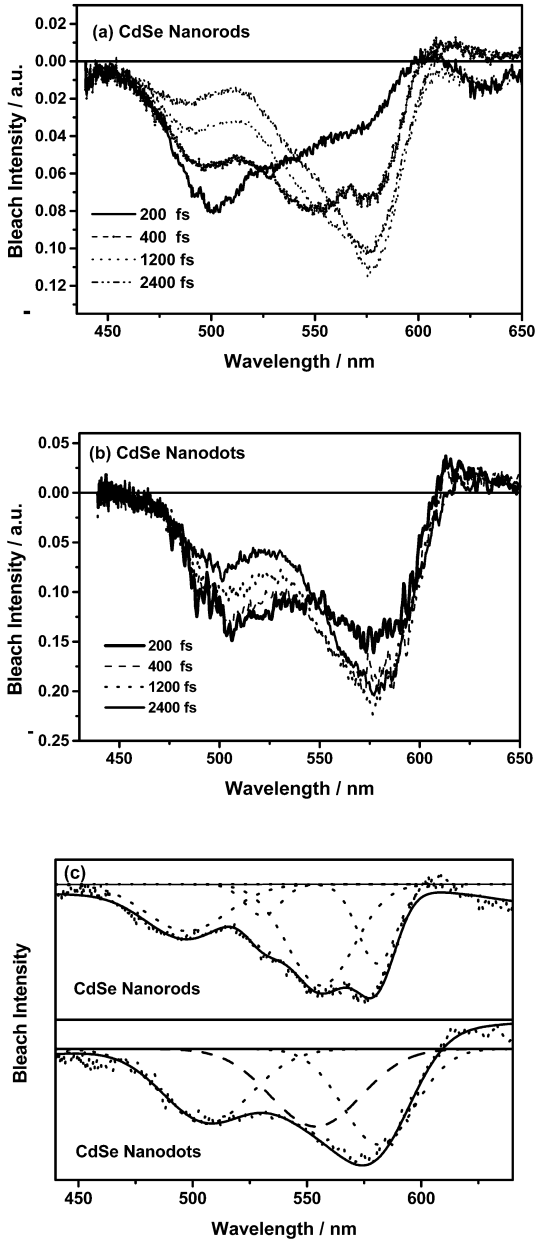

Fig. 5 Shape-dependent ultrafast electron-hole relaxation in CdSe nanocrystals at delay times of 200 fs to 2.4 ps in the spectral range of 440–650 nm. The change in dynamics over the same spectral range is less pronounced for NDs (b) than for the NRs (a). (c) shows the deconvolution of the early time bleach spectra of CdSe NRs and NDs.

have been excited with low laser power (1 μJ) at 400 nm to avoid Auger processes and biexciton formation [30]. The bleach dynamics for the CdSe NRs at several wavelengths between 460 and 600 nm have been monitored. As shown in Fig. 6, the decay becomes faster as the energy decreases. This indicates that the higher states relax much faster than the lower states. Comparing the bleach dynamics of CdSe NRs with the CdSe NDs at the band-gap state (580 nm) shows that the relaxation time of the

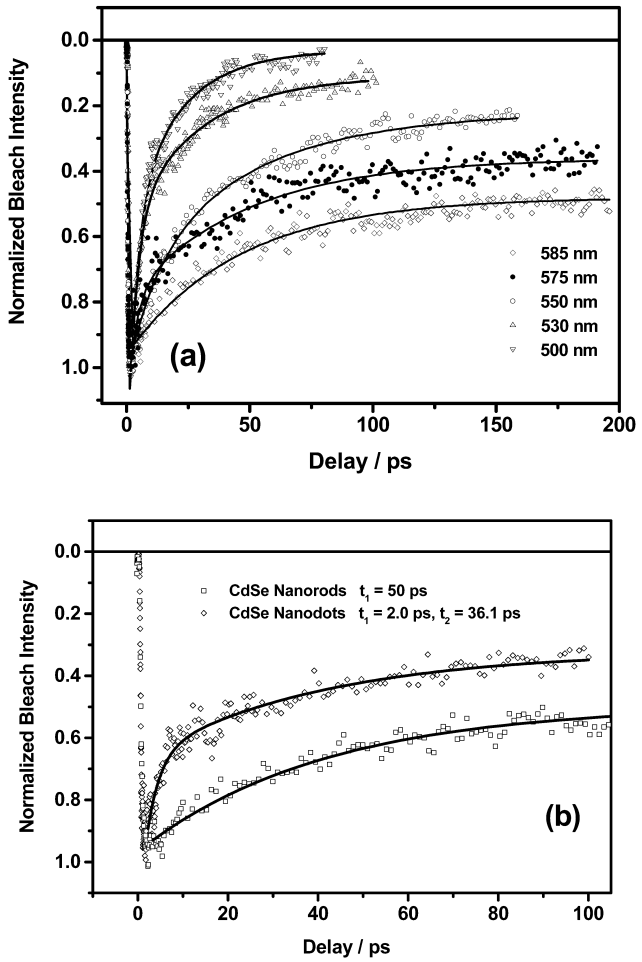

Fig. 6 (a) The decay kinetics of CdSe NRs at different probe wavelengths show that the relaxation is faster for the higher energy states. (b) Comparison between the decay kinetics of the CdSe NRs and NDs at 585-nm wavelength (at the band gap) shows that the decay in case of the NRs is slower than that of the dots.

band-gap state of the NRs is longer than that of the spheres. That might be due to the less-effective surface trapping in the NRs. It has been shown theoretically [24,25] that the geometry not only affects the electronic structure of the semiconductor nanocrystals, but also affects the formation of surface states. The localization of the surface states is induced by the surface curvature. If the particle is ellipsoidal or of rod-like shape, the carrier motion is less restricted along the long axis, whereas on undulating surface, the carrier may be trapped. This might introduce different surface states in the rod-shaped CdSe particles compared to the spherical dots.

METALLIC NANOPARTICLES

Ultrafast electron dynamics in gold nanoparticles embedded in different media

The hot electron dynamics in metallic NPs created by an ultrashort laser pulse have been of great interest [33–35]. Although it was thought that for particles smaller than the electron mean-free path, an enhanced electron-surface scattering should lead to a larger electron–phonon coupling compared to the

bulk, no size and shape dependence of the electron relaxation could be found for gold NPs as small as 5 nm in diameter [33,35] (the electron mean-free path in gold is about 50 nm). This can be understood if the electron-surface scattering is assumed to be mainly elastic owing to the large atomic mass of the gold atoms. These experiments were performed by exciting the electrons with a femtosecond laser pulse and then probing the plasmon absorption band with a second femtosecond laser pulse delayed in time (pump-probe spectroscopy) [33–35]. The hot electrons cause a damping of the plasmon oscillation, which results in a strong bleach signal at the plasmon maximum in the transient absorption spectrum [33–35]. The plasmon bleach recovery hence monitors the cooling dynamics of the hot electrons, which occurs by electron–phonon coupling with the lattice vibrations of the gold NP and also heat transfer to the embedding medium. The relaxation dynamics are found to be strongly dependent on the initial electron temperature (the laser-excitation power). This can be explained by the temperature-dependent heat capacity of the electrons for continuous thin gold films [36]. However, for isolated gold NPs, the question arises as to which role the surrounding medium plays in the overall cooling dynamics and if there is bottleneck occurring. For gold NPs in aqueous solution, apart from an initial fast (few ps) relaxation, a second long decay component of about 100 ps was observed at higher excitation powers [35]. The fast component was therefore assigned to electron–phonon coupling inside the gold NPs, while the long decay component was ascribed to the thermal relaxation with the surrounding medium by phonon–phonon interactions. However, the nature of the coupling to the surrounding matrix at moderate pump energies is still less understood than the electron–phonon coupling observed at low pump intensities. Here, we summarize two experiments in which the electron-cooling dynamics were investigated for gold NPs embedded in different media.

Figure 7 shows the plasmon band bleach recovery dynamics for the same 15-nm gold NPs in solution (iv), in hydrogel (iii), in dimethyl sulfoxide (DMSO) gel (ii), and in dimethylformamide (DMF) gel (i). The sample preparation involving the gold NP synthesis in aqueous solution and the incorporation of the particles in a hydrogel and organo-gel polymer network and the experimental set-up have been described in detail in [37]. The transient signals have been normalized and displaced for comparison and are given as increases in the differential transmission of the probe light ($\Delta T/T$). Figure 7a shows the electron dynamics after excitation with low-power 400-nm femtosecond pulses (120 nJ per pulse). Starting with similar initial electron temperatures, the relaxation dynamics of the plasmon bleach and thus the energy relaxation of the whole system can be directly compared for the different samples. The fast decay component increases from 1.76 ± 0.09 to 2.32 ± 0.08 ps when changing the medium from water to DMSO. In Fig. 7b, a higher excitation power of 750 nJ per pulse was used, which leads to a general increase in the relaxation dynamics and the appearance of a second much slower decay component. However, an increase of the fast relaxation component τ_1 from 2.13 ± 0.06 to 3.76 ± 0.08 ps is again seen when changing the surrounding medium from solution (iv) and hydrogel (iii) to the organic gels [DMSO (ii) and DMF (i)].

The increase in the fast relaxation time τ_1 has been explained by the fact that changing the particle environment leads to a change in the surface properties of the particles. This in turn has a direct influence on the bleach recovery dynamics even at very low pump intensities when the change in the lattice temperature is negligible. It is possible that the surrounding solvent molecules can directly interact with energy levels of the gold NPs. Such a mechanism, known as chemical interface damping, was suggested before in order to explain the plasmon band width as a function of the surrounding medium [38,39].

A more dramatic change in the relaxation dynamics is seen for the slow decay component τ_2 in Fig. 7b. The relaxation time increases from about 150 ps for the solution and the hydrogel sample to 450 ± 40 ps and 1.5 ± 0.23 ns for the DMSO and DMF gels, respectively. The large difference between the relaxation times for the organic gels and the hydrogel can be explained by the difference in the heat conductivities of the different liquids. The heat conductivities of DMSO and DMF are about 3–4 times smaller than the heat conductivity of water [37]. This leads to a longer relaxation time for the particles surrounded by the organic solvent molecules because the heat cannot be effectively removed from the

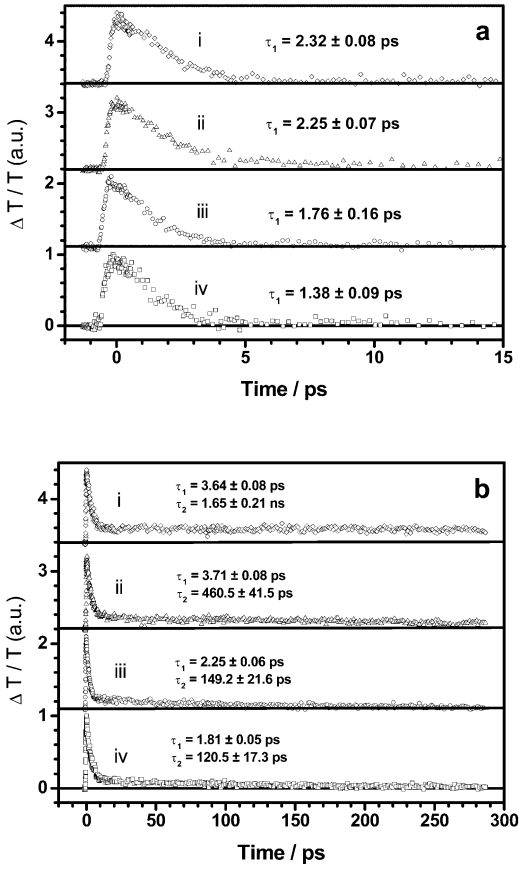

Fig. 7 (a) Plasmon bleach recovery of gold NPs at low pump power in solution (iv), hydrogel (iii), DMF- (ii) and DMSO-organic gel (ii). The excitation wavelength is 400 nm, and the pump power is 120 nJ in all cases. (b) Plasmon bleach recovery of gold NPs at high pump power (750 nJ) in solution (iv), hydrogel (iii), DMF- (ii), and DMSO-organic gel (i). The probe wavelength was chosen as the plasmon absorption maximum in order to achieve maximum sensitivity.

particles through the surrounding matrix by heat conduction. This can explain why the slow component of the plasmon bleach relaxation for gold NPs embedded in an organic gel matrix is much slower compared to the dynamics observed for the same particles in a hydrogel matrix and in aqueous solution.

The difference in heat conductivities, however, cannot account for the difference in the relaxation times observed for the two organic gels (450 ps for DMSO and 1.5 ns for DMF) because the thermal conductivity of DMF is slightly higher than that of DMSO. However, these values are measured for the pure solvents. In this case, the solvent molecules fill out the space in the polymer network, which should result in a different mobility of the molecules compared to the pure solution. One has to consider the possible chemical interaction between the solvent molecules and the NP as well as the polymer (DMF has more tendency to form hydrogen bonds with the *N*-isopropyl-acrylamide molecules) as well as the size of the solvent molecules. DMSO is in fact smaller than DMF. If the heat conduction by the solvent molecules involves not only coupling between their phonon modes but also heat transfer by diffusion of the hot phonons of the solvent away from the NPs, then the mobility of the solvent molecules is very important. (The mobility of the solvent molecules inside the polymer network is not accounted for by

the bulk heat conductivity.) The observed difference can be explained by the lower mobility of the DMSO molecules based on their size and their tendency to interact with the polymer network.

In another experiment, electrochemically synthesized spherical gold NPs were embedded in $MgSO_4$ powder as a solid matrix [40]. This matrix was chosen because it was very different from the liquid media described above and from previously investigated sol-gel films [41]. In particular, due to the larger size of the $MgSO_4$ particles (in the μm size range) surrounding the gold NPs, the thermal contact between the gold NPs and the $MgSO_4$ powder is partially interrupted. Instead, the gold NPs are also surrounded by air. Furthermore, the choice of $MgSO_4$ powder as a matrix allowed us to use femtosecond transient reflectance spectroscopy [42] to probe the electron dynamics after femtosecond laser excitation. Figure 8 shows the change in diffuse reflectance probed at the plasmon maximum at 540 nm for 14.5-nm gold NPs in $MgSO_4$ powder after excitation with 2.70-μJ femtosecond laser pulses at 400 nm (open circles). The diffuse reflectance of the NP-powder composite increases after laser excitation owing to the heating of the electron gas. The subsequent decay corresponds with the cooling of the hot electrons as already discussed above for the gold NPs in aqueous solution and the different gels. The relaxation dynamics are again found to be dependent on the laser pump power and hence the initial electron temperature with a biexponential decay for larger excitation powers. However, in contrast to the system discussed above, the first relaxation time is found to be much longer for the particles in $MgSO_4$ powder. For the case shown in Fig. 8, τ_1 was found to be 9.50 ps (compare this to relaxation times of 1–4 ps in Fig. 7). Even at the lowest excitation powers used for the NP–powder system, we observed longer decay times for τ_1 for this system compared to gold NPs measured in solution or in a gel while τ_2 was found to be of comparable magnitude. In order to test if this difference is due to the change in the environment or may be related to an insufficient sensitivity of the diffuse reflectance set-up, we performed another experiment in which after the measurement of the gold NDs in $MgSO_4$ powder tetrahydrofuran (THF) was added to the sample and the measurement was repeated. The THF replaced the air surrounding the particles, which was clearly visible as bubbles streamed through an upper liquid layer on top of the $MgSO_4$ powder. The result of this experiment is also shown in Fig. 8 (closed squares).

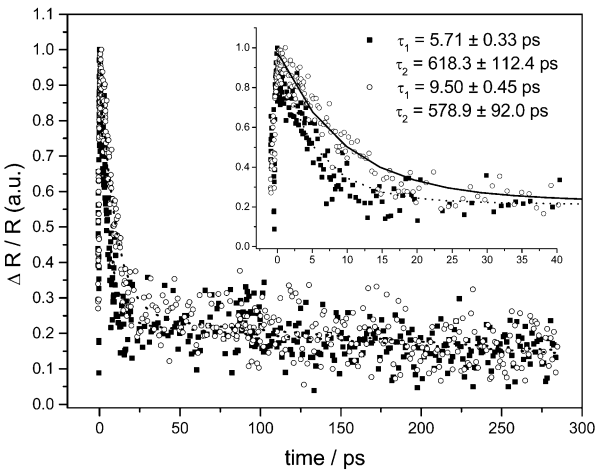

Fig. 8 Plasmon bleach recovery of 14.5-nm spherical gold NPs embedded in $MgSO_4$ powder (open spheres) and after adding THF to the sample (solid squares). The kinetic traces have been normalized for better comparison. Excitation with 2.70 μJ per pulse was carried out at 400 nm and the probe wavelength was set to 540 nm, recording the changes in the transient diffuse reflectance in both cases. While the value for the fast decay component decreases from 9.50 to 5.71 ps upon the addition of the solvent, the slow component remains unchanged. This is more clearly seen in the inset, which shows the dynamics of the plasmon bleach recovery on a shorter time scale.

While the fast decay component decreases by about a factor of 2 from 9.50 to 5.71 ps upon the addition of the solvent, the slow components are comparable considering the experimental error. This is more clearly seen in the inset, which shows the dynamics of the plasmon bleach recovery on a shorter time scale.

The results shown in Fig. 8 can be explained by the incomplete thermal contact between the gold NPs and the $MgSO_4$ powder. This partially hinders the heat transfer from the hot particles to the powder particles, which are in direct contact with the gold NPs. Upon addition of a solvent (THF) the thermal contact is improved, and the deposited laser energy can be transferred to the solvent now. This leads to an increase of the fast relaxation time by a factor of two.

In summery, we have shown two examples in which the surrounding medium has a significant effect on the cooling dynamics of hot electrons in gold NPs created by a femtosecond laser pulse. Both of the two decay components of the plasmon bleach recovery are influenced by the surrounding medium. In general, the recovery times become slower when the thermal contact between the particles and the matrix is decreased (as in the $MgSO_4$ powder system) or when the thermal conductivity of the medium is decreased (as in the series with the hydrogel compared to the organic gels). These results confirm that the surface properties of the metallic NPs and the thermal properties of the surrounding medium play important roles in the cooling dynamics of the hot carriers in metallic NPs. Similar results have been obtained by Bigot et al. [43], who measured the relaxation dynamics of 6.5-nm silver NPs embedded in two different types of transparent glasses (alumina and glass). They also found an increase of the electron–phonon relaxation time from 0.77 to 1.4 ps when comparing the alumina and glass matrices, respectively. They explained their results in terms of the better heat conductivity of the alumina. An interesting study was also recently reported by Westcott et al. [44], who showed that the chemical nature of surface-adsorbed molecules could have an effect on the electron dynamics of gold core-shell NPs. They found that the molecules providing the strongest change in the dynamics decreasing the electron relaxation lifetime from 2.7 to 1.7 ps possess the largest induced dipole moments near the metal surface. More experiments are necessary to elucidate the mechanism involved in the heat transfer from the gold NPs to the surrounding matrix (i.e., the type of phonons involved). Apart from the role of the embedding medium on the electron dynamics in metal NPs it is also a very important question to understand the influence of other metal NPs in close proximity of each other. This is the case in assembled structures of NPs. Results on the assembly of gold NRs are given in the next section.

Self-assembly and surface-enhanced Raman scattering (SERS) of gold nanorods

Gold NRs are grown in a surfactant template of hexadecyltrimethyl ammonium bromide (CTAB). Studies show that the CTAB molecules form a membrane structure around NRs and produce particles with positive surface charges [45]. FTIR and Raman studies show that the hydrophobic part of the membrane lacks a crystalline structure at room temperature owing to the free rotation of the methylene chains. At the interface of the metal-molecules, the head group of the surfactant (quaternary nitrogen) binds to the gold atoms via the bromide counter ion. Thermogravimetric analysis (TGA) studies show that the surfactant-capped NRs have three different desorption temperatures at 230, 273, and 344 ºC. Based on the bilayer structure, the first desorption is attributed to the surfactant monomers, which are weakly bound to the outer layer. The second and third desorption temperatures are attributed to the outer and inner layers of the membrane, respectively. TEM shows that the third desorption temperature coincides with the shape transformation from NRs to nanospheres (NSs). Based on the crystallographic studies on these particles [46], gold NSs possess two types of {111} and {100} facets, while NRs have an additional {110} facet, which has a higher surface energy [47]. The higher energy of this facet results in stronger binding to the surfactant and stabilization of this facet in NRs. Upon heating and removal of the capping at 344 ºC, the unstable {110} facet starts to reconstruct to more stable facets, and, therefore, shape transformation takes place.

In packing and assembly of objects in macroscale, size and shape homogeneity are two dominant factors. However, in nanoscale, the assembly process becomes more complicated owing to the surface structure of the particles and the development of Columbic and Van der Waals forces.

For particles with hydrophilic surfaces dispersed in a thin layer of an aqueous solution, the capillary forces start to manifest when the thickness of the water layer becomes equal to the particle diameter [48]. As the top of the particles protrude from the water layer, perturbation of the meniscus around a particle by the presence of another particle causes a net attractive force between the two particles. These forces originally were observed between particles with dimensions larger than 0.01 cm (floating capillary forces) and later for latex particles of 1 μm (immersion capillary forces) [49].

In the case of gold NRs smaller than 100 nm, our self-assembly results showed that the immersion capillary forces can overcome the thermal energy of the environment (kT) and are present in such small particles [50]. For NRs confined in a thin layer of water, TEM images show that particles form colonies of assembled particles. Depending on the rate of water evaporation, these colonies could be more organized and larger in size, see Figs. 9a and 9b. In this process, owing to water evaporation, NRs protrude from the solution and if their concentration is suitable, the attractive capillary forces drive them toward organized structure. Due to the NR shape anisotropy, these forces are stronger when NRs approach each other by side.

In order to extend the size of the assemblies, a substrate was half-inserted into 100 μl of an NR solution inside a small container as shown in Fig. 9c. A TEM image of the interface of such a substrate is shown in Fig. 9e. It can be seen that the packing of NRs mainly takes place at the interface of the substrate/solution/air (called the leading edge). By insertion of the substrate into the solution, a thin layer of the solution forms parallel to the plane of the substrate due to the surface tension. Upon protrusion of the particles confined in the thin layer on the substrate, particle packing starts at the leading edge. Moreover, the water evaporation (Fig 9d, arrow 3) at the leading edge results in formation of a pressure gradient, which directs flow from the bulk solution toward the leading edge (see Fig. 9d, arrows 1 and 2). This gradient results in a convective current, which drives the NRs from the bulk solution to the front line of the assembly. The rate of water evaporation is crucial. If it is fast, the friction between the particles and the substrate overweights the capillary forces, and particles cannot assemble properly. Examples of different evaporation rates are shown in Figs. 9f, 9g, and 9h.

An interesting aspect of the metal NPs both in pure and applied sciences is their different and often enhanced optical properties with respect to their bulk materials. As an example, gold NRs used in our studies contain 10^5–10^6 atoms, which represents a significant polarizability $P = n \bullet p$, where n is the number of free electrons per unit volume and p is the dipole moment. In-phase excitation of the collection of these electrons (plasmon) with an incident light generates an electric field on the particle surface, which is proportional to the dielectric of the metal and its volume [38]. This enhanced field is a new property, which is absent in the bulk gold. When molecules (strongly) adsorb to the surface of metallic particles in the size range of 10–100 nm, the Raman scattering of some of the molecular vibrations are enhanced millions of times. This property is also found in other noble and some of the alkali metals [51].

In the original SERS studies, these active substrates were used as rough features on metal surfaces, later they were used in the form of colloidal particles and their aggregates [52]. Although a full explanation of this effect remains an open question, there are many reports on elucidating different aspects. Two effects involved in this process are electromagnetic [51] and chemical effects [39]. If $P = \alpha \bullet E$, where P is the induced dipole moment, α the polarizibility of the adsorbed molecule, and E is the field experienced by the molecule, the chemical effect can be viewed as the factors that influence the polarizability of the adsorbed molecule. More recent models involving the electronic interaction of the metal and molecule have been proposed in explaining this effect [39,53].

In the electromagnetic effect, for the adsorbed molecule, the overall field is the sum of the one on the surface of the particle and the incident field, i.e., $E_p + E_i$. Both theory and experiment have con-

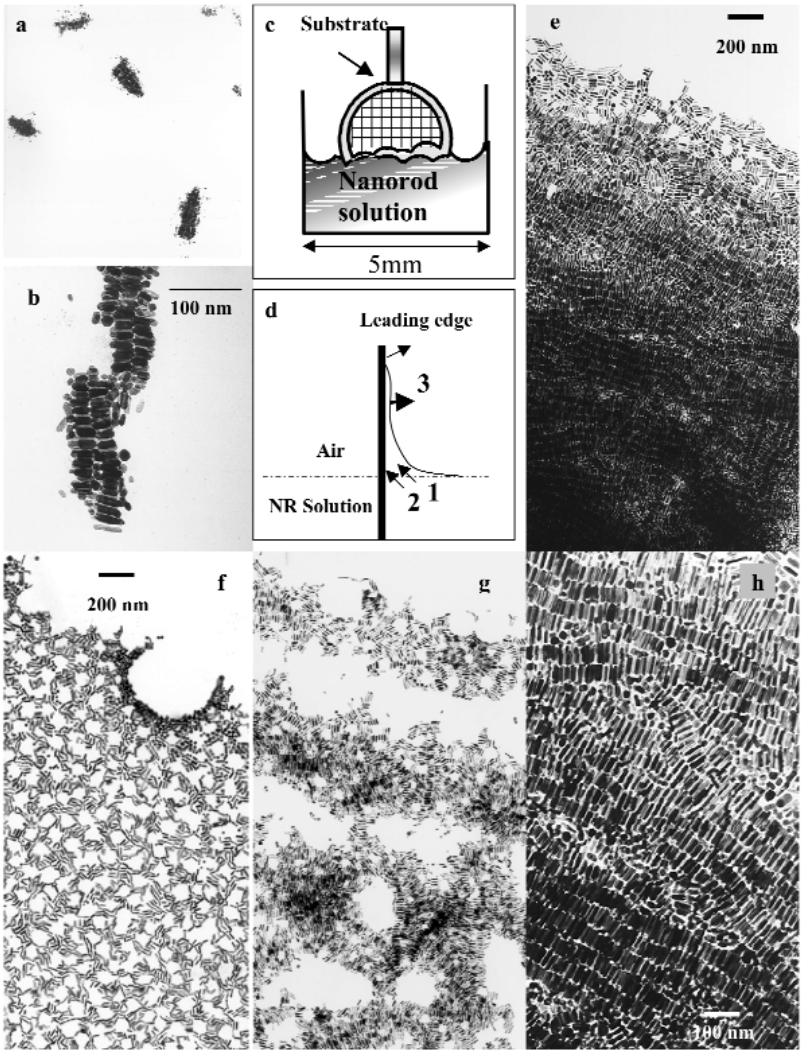

Fig. 9 (a) Result of self-assembly from a thin layer of NR solution under slow evaporation. Particles form colonies of assembled particles due to the capillary forces. (b) One of the assemblies in part (a) in a larger magnification. Side-by-side assembly is the common type of packing. (c) Scheme of the incomplete immersion of the substrate into the NR solution. The substrate was kept at a fixed position until the complete water evaporation. (d) This cartoon represents the thin layer formed on the substrate and its connection to the bulk solution. The evaporation of the water from the thin layer (arrow 3) results in particle protrusion and appearance of the lateral capillary forces. This evaporation also results in a pressure gradient (shown by arrows 1 and 2), which moves the NRs toward the leading edge of the assembly. (e) TEM image of the assembled particles at the leading edge (contact line of substrate/solution/air). The fast evaporation of the water from the thin layer increases the friction between the particles and substrate. (f), (g), and (h) represent three regions with different rates of evaporation.

firmed that the field is maximized when the excitation source is in resonance with the plasmon frequency [54].

Colloidal particles (both spherical and spheroidal) are appropriate systems for testing the theoretical models developed for explaining the origin of the SERS effect due to their shape homogeneity. Most of the experimental work reported in the literature is related to the spherical particles, while stud-

ies on rod-shaped particles (spheroidal) in solution are absent. Development in the synthesis of NRs opened up the opportunity to explore the Raman enhancement properties of these particles. In the following section, the SERS activity of NRs will be compared with that of NSs.

Gold NRs with dimensions of 10×25 nm have a transverse and a longitudinal plasmon band at 520 and 695 nm, respectively, while NSs have only one plasmon band located at about 520 nm. The SERS activity of gold NRs and gold NSs have been studied when a near IR (1064 nm) Nd:YAG laser was used for excitation [55]. Figure 10i shows the visible absorption spectra of the NRs, NSs and surfactant solution (CTAB), and the wavelength of the excitation laser. Figure 10j illustrates their SERS spectra. For NRs, the concentration of the adsorbed surfactant to the surface is about 10^{-5} M. The intense and broad peak at 174 cm^{-1} is the Au–Br vibration, and the rest belongs to the methylene and methyl groups' vibrations of the head group. For the surfactant solution (0.08 M), no Raman peaks are observed. In fact, even the Raman spectrum of the pure surfactant has lower peak intensities relative to the enhanced peaks. Note that the excitation is far from the surface plasmon band of both NRs and NSs, but strong SERS activity is seen only in NRs. In addition to the capping material, other molecules can also be adsorbed to the gold NRs for SERS studies.

The estimated enhancement factors (EFs) for surfactant molecules and pyridine were found to be 10^4 and 10^5, respectively [55], while the calculated EF using the electrodynamic theory of Wang and Kerker [54] for the ring vibration of the pyridine was found to be 1000. In this calculation, the Au–N distance was assumed to be 1 Å, and the excitation wavelength was 1064 nm. The discrepancy was attributed to the absence of the chemical effect in this model. The requirement for having such an effect is the strong binding of the molecules to the metal surface. This condition is present in NRs owing to the higher surface energy of the {110} facet. In fact, the stronger SERS activity of NRs relative to NSs is attributed to the stronger binding of the molecules to the {110} facets (this facet is absent in NSs)

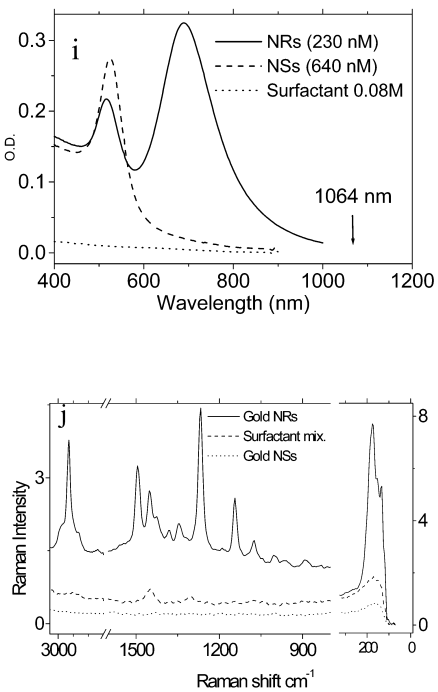

Fig. 10 (i) Visible absorption of gold NRs, NSs, and 0.08-M surfactant solution. (j) The SER spectra of the surfactant molecules on the gold surface for NRs and NSs and the Raman spectrum of the surfactant solution without any clear peaks. The excitation wavelength is shown with an arrow.

[55]. The partial plasmon excitation in NRs is considered the second reason for the higher activity, which can also be inferred from the estimated EF using the theoretical model [54].

ACKNOWLEDGMENTS

This work was supported by the DMR division of NSF (Grant No. 3306A15).

REFERENCES

1. J. Z. Zhang. *Acc. Chem. Res*. **30**, 423 (1997).
2. H. Weller and A. Eychmüler. In *Advances in Photochemistry*, pp. 165–215, Wiley, New York, 20 (1995).
3. A. P. Alivisatos. *J. Phys. Chem B* **100**, 13226 (1996).
4. (a) M. Kerker. *The Scattering of Light and Other Electromagnetic Radiation*, Academic, New York (1969); (b) C. F. Bohren and D. R. Huffman. *Absorption and Scattering of Light by Small Particles*, Wiley, New York (1983).
5. For recent reviews see: (a) S. Link and M. A. El-Sayed. *J. Phys. Chem. B* **103**, 8410 (1999); (b) M. A. El-Sayed. *Acc. Chem. Res.* **34**, 257 (2001); (c) S. Link and M. A. El-Sayed. *Int. Rev. Phys. Chem.* **19**, 409 (2000).
6. A. Henglein *J. Phys. Chem*. **97**, 8457 (1993).
7. C. B. Murray, D. J. Norris, M. G. Bawendi. *J. Am. Chem. Soc*. **115**, 8706 (1993).
8. E. Lifshitz, I. Dag, I. D. Litvitn, G. Hodes. *J. Phys. Chem. B* **102**, 9245 (1998).
9. T. Vossmeyer, G. Reck, L. Katsikas, E. T. K. Haupt, B. Schultz, H. Weller. *Science* **267**, 1476 (1995).
10. N. Herron, J. C. Clabrese, W. E. Farneth, Y. Wang. *Science* **259**, 1426 (1993).
11. V. Soloviev, A. Eichhöfer, D. Fenske, U. Banin. *J. Am. Chem. Soc.* **122**, 2673 (2000).
12. V. N. Soloviev, A. Eichhöfer, D. Fenske, U. Banin. *Phys. Stat. Sol. B* **224**, 285 (2001).
13. K. Eichkorn and R. Ahlrichs. *Chem. Phys. Lett.* **288**, 235 (1998).
14. M. A. Hines and P. Guyot-Sionnest. *J. Phys. Chem. B* **100**, 468 (1996).
15. X. Peng, L. Manna, Y. Weidong, J. Wickham, E. Scher, A. Kadavanich, A. P. Alivisatos. *Nature* **407**, 981 (2000).
16. L. Manna, E. C. Scher, A. P. Alivisatos. *J. Am. Chem. Soc.* **122**, 12700 (2000).
17. Z. Peng and X. Peng. *J. Am. Chem. Soc*. **123**, 1389 (2001).
18. A. W. Castleman and K. H. Bowen. *J. Phys. Chem.* **100**, 12911 (1996).
19. S. H. Tolbert and A. P. Alivisatos. *Science* **265**, 373 (1994).
20. C. F. Landes, C. B. Burda, M. Braun, M. A. El-Sayed. *J. Phys. Chem. B* **105**, 2981 (2001).
21. C. F. Landes, M. Braun, M. A. El-Sayed. *J. Phys. Chem. B* **105**, 10554 (2001).
22. C. F. Landes, C. Burda, M. Braun, M. A. El-Sayed. *Nano Lett.* **1**, 667 (2001).
23. C. B. Murray, C. R. Kagan, M. G. Bawendi. *Annu. Rev. Mater. Sci.* **30**, 545 (2000).
24. G. Cantele, D. Ninno, G. Iadonisi. *J. Phys.: Condens. Matter* **12**, 9019 (2000).
25. G. Cantele, D. Ninno, G. Iadonisi. *Nano Lett.* **1**, 121 (2001).
26. L.S. Li, J. Hu, W. Yang, A. P. Alivisatos. *Nano Lett*. **1**, 349 (2001).
27. J. Hu, L.-S. Li, W. Yang, L. Manna, L.-W. Wang, A. P. Alivisatos. *Science* **292**, 2060 (2001).
28. J. Hu, L.-W. Wang, L.-S. Li, W. Yang, A. P. Alivisatos. *J. Phys. Chem. B* **106**, 2447 (2002).
29. Z. A. Peng and P. A. Xiaogang. *J. Am. Chem. Soc*. **123**, 1389 (2000).
30. M. B. Mohamed, C. Burda, M. A. El-Sayed. *Nano Lett*. **1**, 589 (2001).
31. V. I. Klimov. In Handbook of *Nanostructured Materials and Nanotechnology*, H. S. Nalwa (Ed.), Vol. 4: *Optical Properties*, Academic, NY (2000).
32. J. K. Hodak, A. Henglein, G. V. Hartland. *J. Phys. Chem. B* **104**, 9954 (2000).
33. J.-Y. Bigot, V. Halte, J.-C. Merle, A. Daunois. *Chem. Phys.* **251**, 181 (2000).

34. N. Del Fatti, F. Vallee, C. Flytzanis, Y. Hamanaka, A. Nakamura. *Chem. Phys.* **251**, 215 (2000).
35. S. Link and M. A. El-Sayed. *J. Phys. Chem. B* **103**, 8410 (1999).
36. C.-K. Sun, F. Vallee, L. H. Acioli, E. P. Ippen, J. G. Fujimoto. *Phys. Rev. B* **50**, 15337 (1994).
37. M. B. Mohamed, T. S. Ahmadi, S. Link, M. Braun, M. A. El-Sayed. *Chem. Phys. Lett.* **343**, 55 (2001).
38. U. Kreibig and M. Vollmer. *Optical Properties of Metal Clusters*, Springer, Berlin (1995).
39. B. N. J. Persson. *Surf. Sci*. **281**, 153 (1993).
40. S. Link, A. Furube, M. B. Mohamed, T. Asahi, H. Masuhara, M. A. El-Sayed. *J. Phys. Chem. B* **106**, 945 (2002).
41. M. Perner, P. Bost, G. v. Plessen, J. Feldmann, U. Becker, M. Mennig, H. Schmidt. *Phys. Rev. Lett*. **78**, 2192 (1997).
42. T. Asahi, A. Furube, H. Fukumura, M. Ichikawa, H. Masuhara. *Rev. Sci. Instrum.* **69**, 361 (1998).
43. V. Halte, J.-Y. Bigot, B. Palpant, M. Broyer, B. Prevel, A. Perez. *Appl. Phys. Lett.* **75**, 3799 (1999).
44. S. L. Westcott, R. D. Averitt, J. A. Wolfgang, P. Nordlander, N. J. Halas. *J. Phys. Chem. B* **105**, 9913 (2001).
45. B. Nikoobakht and M. A. El-Sayed. *Langmuir* **17**, 6368 (2001).
46. Z. L. Wang, M. B. Mohammed, S. Link, M. A. El-Sayed. *Surf. Sci*. **440**, L809 (1999).
47. Z. L. Wang, R. P. Gao, B. Nikoobakht, M. A. El-Sayed. *J. Phys. Chem. B* **104**, 5417 (2000).
48. P. A. Kralchevsky, N. D. Denkov, V. N. Paunov, O. D. Velev, I. B. Ivanov, H. Yoshimura, K. Nagayama. *J. Phys.: Condens. Matter* **6**, A395 (1994).
49. N. D. Denkov, O. D. Velev, P. A. Kralchevsky, I. B. Ivanov, H. Yoshimura, K. Nagayama. *Nature* **361**, 26 (1993).
50. B. Nikoobakht, Z. L. Wang, M. A. El-Sayed. *J. Phys. Chem. B* **104**, 8635 (2000).
51. M. Moskovits. *Rev. Mod. Phys.* **57**, 783 (1985).
52. J. A. Creighton, C. G. Blatchford, M. G. Albercht. *J. Chem. Soc., Faraday Trans. 2* **75**, 790 (1979).
53. A. M. Michaels, M. Nirmal, L. E. Brus. *J. Am. Chem. Soc.* **121**, 9932 (1999).
54. D. S. Wang and M. Kerker. *Phys. Rev. B* **24**, 1777 (1981).
55. B. Nikoobakht, J. Wang, M. A. El-Sayed. *Chem. Phys. Lett*. In press.